MULTIPHYSICS SIMULATION OF SPATIAL-TEMPORAL BEAM SHAPING IN LASER POWDER BED FUSION USING OPENFOAM

B. ZHOU*, J. BARODE*, V. K. NADIMPALLI*, A. BAUCH**, D. HERZOG***, J. H. HATTEL*, M. BAYAT*

**Technical University of Denmark, Department of Mechanical Engineering, 2800, Kgs. Lyngby, Denmark, baozh@dtu.dk*
***Fraunhofer Research Institution for Additive Manufacturing Technologies IAPT, 21029, Hamburg, Germany*
****Hamburg University of Technology, Institute for the Industrialization of Smart Materials, 21029, Hamburg, Germany*

DOI 10.3217/978-3-99161-089-2-011, license CC BY 4.0

ABSTRACT

Metal additive manufacturing (MAM) has been applied in various advanced fields due to its flexibility and superiority in producing complex geometries, compared to subtractive manufacturing methods. The powder bed fusion using a laser beam (PBF-LB) process, as a major subbranch of MAM, involves multiple complex physical phenomena, e.g. phase changes, buoyancy, surface tension, evaporation, Marangoni effects, melting, solidification, and microstructural evolution. The interplay between process settings and melt-pool conditions has a significant influence on part quality. Multiphysics simulations that incorporate these phenomena are considered as a robust and reliable tool to study this complex interplay. This study simulates the PBF-LB process for copper and stainless steel 316L (SS 316L) under infrared laser irradiation at the deposition scale, using the open-source code OpenFOAM. The simulation results demonstrate good agreement with benchmark experimental data in terms of the transverse cross-section profiles of the melt regions when applying spatial and temporal beam shaping in PBF-LB. These beam shaping techniques are efficient ways to adjust the melt-pool morphology and eventually to improve the print quality. In this study, continuous Gaussian and ring-shaped laser beam profiles, and pulsed beam shaping techniques are modelled, and their effects on the melt pool are investigated. Moreover, for copper, there has been long controversy in the literature in terms of the correct absorption rate of laser radiation. We hence explore the influence of absorptivity on the melt-region cross-sectional dimension. This work focuses on simulating the melt pool on metal substrates and offers insights into the fundamental impacts of the process settings on melting behavior and absorptivity while using beam shaping.

Keywords: PBF-LB, Metal Additive Manufacturing, Absorptivity, Melt Pool, Beam Shaping

INTRODUCTION

Metal additive manufacturing (MAM), involving multi-scale and multi-disciplinary phenomena, has emerged in many engineering fields, including the fabrication of aerospace components [1], biomedical instruments [2] and various complex products [3]. Numerical simulations and experimental measurements are two common approaches for studying the thermal, mechanical and fluid dynamic behaviors involved during MAM process. While experiments provide critical benchmarks for validation, simulations enable efficient and cost-effective exploration of parameter spaces.

Among numerical methods, finite volume method (FVM)-based open-source tools such as OpenFOAM [4] have been extensively used for computational fluid dynamics (CFD) simulations [5]. In numerical models of powder bed fusion using a laser beam (PBF-LB), early studies primarily focused on pure conduction modes, later evolving into more comprehensive investigations that incorporated fluid dynamics. In conduction-based models, some researchers addressed purely thermal problems [6-7], while others took into account thermal-mechanical coupling effects [8-9]. Current simulations are usually able to capture a range of physical phenomena, including melting, solidification and evaporation. They are mathematically modelled using mass, momentum, and energy conservation conditions, often with additional surface-tracking methods to account for free-surface deformation [10]. The melt and solid phases are typically identified using threshold temperatures: regions above the liquidus point are considered molten, while those below the solidus temperature are treated as solid. Recent developments such as beamWeldFoam [11] and laserBeamFoam [12-13] within the OpenFOAM framework have enabled simulation of complex phenomena including Marangoni effects, recoil pressure, laser absorptivity calculations using Fresnel equations [14], and multi-laser and multi-material interactions [15].

Copper, due to its high reflectivity and thermal conductivity, encounters unique challenges during the PBF-LB process. Its laser absorption is influenced by multiple factors, including temperature, incident laser intensity, laser wavelength, surface roughness, contamination, and oxidation of the material surface [16]. Accurately predicting copper's absorptivity is both difficult and critical for reliable simulation and process optimization. Reported absorption rates vary widely across the literature. For example, Alphonso et al. [17] reported absorptivity values of 12% for laser radiation in the (near-) infrared spectrum and 40% in the green spectrum. Gargalis et al. [18] recommended around 20% for conduction mode and 53% for keyhole welding [19]. Nordet et al. [20] cited values as low as 4%-5% for laser radiation at a wavelength of around 1070 nm.

Beam shaping is a promising strategy for enhancing the quality of PBF-LB products, encompassing both spatial and temporal modifications. Spatial shaping involves modifying the laser beam profile, with commonly used shapes such as Gaussian [21], ring-shaped [22], tophat [23], and elliptical [24] profiles. They have different influences on melt-pool morphology and defect formation. Gaussian beams, though widely used, tend to concentrate energy at the center, which may cause unwanted spatter and degrade print quality [25]. In contrast, the ring-shaped profile redistributes the beam intensity, thus reducing the spatter [26], affecting surface roughness and porosity [27]. Galbusera et al. [28] showed that the core-to-ring power ratio greatly influences porosity formation, a trend also observed by Hayat et al.

[29] using elliptical and square beam profiles during laser welding of aluminium alloys. Temporal beam shaping involves modulating the laser's on and off state over time. During this process, two key control parameters are the duty cycle which is the ratio of the laser on-time to the cycle time, and the laser switching frequency [30]. From the relevant work presented by Bayat et al. [31], it is observed that these parameters significantly affect track morphology, with distinctive fish-fin surface topologies appearing at low cycle periods. Similar surface features were reported by Zheng et al. [32], who also noted that longer exposure time could produce denser fish-scale patterns. Despite these findings, studies focusing on beam shaping for copper and comparative investigations across different metals remain limited.

In this study, we extend the open-source codes laserBeamFoam [12] which originally included a continuous Gaussian laser beam, to work on temporal and spatial beam shaping, and develop a multiphysics numerical model to simulate the metal PBF-LB process. The numerical model is validated against benchmark data for several cases: continuous Gaussian and ring-shaped lasers on copper, and a pulsed Gaussian laser on stainless steel 316L (SS 316L). Based on the validated framework, we explore the influence of absorptivity on the melt-pool dynamics of copper, presenting absorptivity vs. deviation plots for various laser profiles. The spatial and temporal beam shaping effects on material deposition patterns are investigated as well. The rest of this paper unfolds as follows. The second section describes simulation models, as well as the temporal and spatial beam shaping techniques. The third section presents validation of the simulation by comparison with benchmark results. The fourth section discusses the laser absorptivity of copper and analyzes the influence of beam shaping. The fifth section concludes the paper.

NUMERICAL MODEL

GOVERNING EQUATIONS

In numerical simulation of PBF-LB, different assumptions can lead to different forms of the governing equations which generally describe the mass, momentum, and energy conservation conditions of the fluid-thermal field, as well as interface capturing methods. Within the framework of the codes laserBeamFoam [12], the fluid momentum conservation is described by the Navier-Stokes equations

$$\frac{\partial(\rho u_i)}{\partial t} + \frac{\partial(\rho u_i u_j)}{\partial x_j} = -\frac{\partial P}{\partial x_j} + \frac{\partial \tau_{ij}}{\partial x_j} + F_i^b + F_i^s + S_i^D, \tag{1}$$

where the terms in the left-hand side represent transient and convective terms, and those in the right-hand side are the pressure gradient, the viscous term, the buoyancy force F_i^b, the surface force F_i^s, and the Darcy sink term S_i^D. In Eq. (1) ρ, P, t denote the density, pressure and time, u_i, x_i the velocity and space coordinate, and τ_{ij} the viscous stress tensor. i, j both take values

from 1 to 3. For an incompressible flow which is described by a velocity divergence-free condition

$$\frac{\partial u_i}{\partial x_i} = 0, \tag{2}$$

the viscous stress tensor is $\tau_{ij} = \rho\nu\left(\frac{\partial u_i}{\partial x_j} + \frac{\partial u_j}{\partial x_i}\right)$. Here, ν is the kinematic viscosity. The surface force F_i^s includes the surface tension, the recoil force due to vaporization, and the Marangoni force, i.e.,

$$F_i^s = \left[\sigma\kappa n_i + P^r n_i + \frac{\partial\sigma}{\partial T}\left(\frac{\partial T}{\partial x_i} - n_i\left(\frac{\partial T}{\partial x_j}n_j\right)\right)\right]|\nabla\alpha|\frac{2\rho}{\rho_1+\rho_2}, \tag{3}$$

where σ, κ, T, α are the surface tension coefficient, the curvature, the temperature and the volume fraction of dense phase. ρ_1, ρ_2 are the density of dense material and gas. n_i is the x_i-direction component of normal vector. The recoil pressure P^r is computed by

$$P^r = 0.54p_0 e^{\frac{L^v M(T-T^v)}{RT^v T}}, \tag{4}$$

where T^v, M, L^v, R are the temperature at the boiling point, molar mass, latent heat due to vaporization and universal gas constant, respectively. p_0 is the vapor pressure. The buoyancy force F_i^b is computed by the Boussinesq approximation

$$F_i^b = -\varepsilon_1\rho g\delta_i\beta(T - T^s), \tag{5}$$

where g, β and T^s are the gravitational acceleration, the thermal expansion coefficient, and the solidus temperature, respectively. ε_1 is a temperature sensitivity coefficient, which is calculated by

$$\varepsilon_1 = \begin{cases} 0, & T < T^s \\ \frac{T-T^s}{T^l-T^s}, & T^s \le T \le T^l \\ 1, & T > T^l \end{cases}. \tag{6}$$

Here, T^l denotes the liquidus temperature. In Eq. (5) the tuning coefficient $\delta_i = 1$ when the buoyancy F_i^b points in the direction of gravity, otherwise $\delta_i = 0$. The Darcy sink term is computed by

$$S_i^D = -\frac{C_1(1-f_l)^2}{f_l^3 + C_2}u_i, \tag{7}$$

where C_1 is a constant multiplier which here takes a large value 10^6 and f_l is the liquid fraction with the value of 0 in the solid state and 1 in the liquid. To avoid the case where the denominator is zero, a small positive parameter C_2 is applied, and here $C_2 = 10^{-12}$. At the solid state, $u_i = 0$ and $f_l = 1$ give $S_i^D = 0$.

To capture the interface between the metal and gas phases, the volume of fluid (VOF) method [33] is applied, which is mathematically described by

$$\frac{\partial \alpha}{\partial t} + \frac{\partial (\alpha u_i)}{\partial x_i} = 0. \tag{8}$$

$\alpha = 1$ represents the pure dense material, $\alpha = 0$ the pure gas, and $0 < \alpha < 1$ the interface.

The energy conservation is formulated by the temperature field

$$\frac{\partial (\rho c^p T)}{\partial t} + \frac{\partial (u_i \rho c^p T)}{\partial x_i} - \frac{\partial}{\partial x_j}\left(k \frac{\partial T}{\partial x_i}\right) = S^H - Q^v - Q^f, \tag{9}$$

where c^p is the specific heat, k the thermal conductivity. S^H is the external heat source. Q^v, Q^f are the latent heat due to vaporization and fusion, respectively, which are calculated by

$$Q^v = 0.82|\nabla \alpha| \frac{L^v M p_0}{\sqrt{2\pi MRT}} e^{\frac{L^v M (T - T^v)}{RT^v T}}, \tag{10}$$

and

$$Q^f = L^f \left[\frac{\partial (\rho \varepsilon_1)}{\partial t} + \frac{\partial (\rho u_i \varepsilon_1)}{\partial x_i}\right], \tag{11}$$

where L^f is the latent heat of fusion. The heat source S^H is provided by an external laser, which is the product of laser power q^{laser} and absorptivity η, i.e. $S^H = \eta q^{laser}$. The formulation of the laser source q^{laser} is presented in Eq. (13).

After each time step is calculated, the relevant physical properties Υ are updated generally by

$$\Upsilon = \alpha \Upsilon_1 + (1 - \alpha)\Upsilon_2, \tag{12}$$

where Υ_1 represents the property of dense material phase, with Υ_2 the property of the gas phase. Here, the physical properties involved include ρ, T^s, T^l, β, ν, l^f, c^p and k.

SPATIAL AND TEMPORAL BEAM SHAPING

In this work, we apply the lasers with Gaussian and ring-shaped laser beam profiles, as shown in Fig. 1.

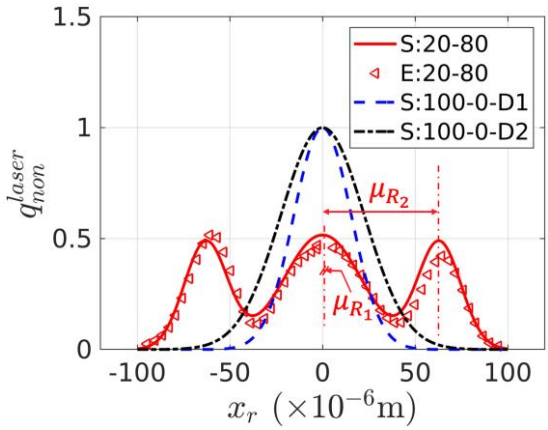

Fig. 1 One-dimensional Gaussian and ring-shaped beam shapes. q_{non}^{laser} denotes the normalized power intensity, and x_r represents the radial position. μ_{R1} and μ_{R2} denote the central position of the core and the ring

In the legend, S denotes the beam shapes which are applied in our simulations, calculated by Eq. (13) and E denotes the shape used in the referenced experiment [34], and the following number denotes the power ratio of the core to the ring. D1 and D2 denote the diameter of the two Gaussian shapes, respectively. For example, S:100-0-D1 represents the pure Gaussian laser with a diameter of D1 used in the simulations. In the simulation, these shapes are analytically expressed by

$$q^{laser} = H(t)\frac{Q}{\pi(1+a_r)}\left[\frac{1}{\sigma_c^2}e^{-\frac{(d-\mu_{R1})^2}{\sigma_c^2}} + \frac{a_r}{2\sqrt{2}\omega\mu_{R2}\sigma_r}e^{-\frac{(d-\mu_{R2})^2}{\sigma_r^2}}\right], \tag{13}$$

where ω is an adjustable factor, and Q is the nominal laser power with unit of W. a_r is used to calculate the weight coefficient of the ring power ratio. μ_{R1} and μ_{R2} denote the central position of the core and the ring, as shown in Fig. 1. σ_c and σ_r are the variance of the core and the ring. θ is the incident angle of the laser beams. d describes the position of the laser, which is defined by

$$d = \sqrt{\left(x - b_g\right)^2 + \left(z - l_g - vt\right)^2} \tag{14}$$

where b_g and l_g are used to define the initial position of the laser in the x and z directions, and v is the laser scanning speed. In Eq. (13), $H(t)$ is a time-dependent function which controls the on and off of the power. For example, in Fig. 2(a), when the laser provides a continuous source of power, $H(t) = 1$ during the whole simulation process.

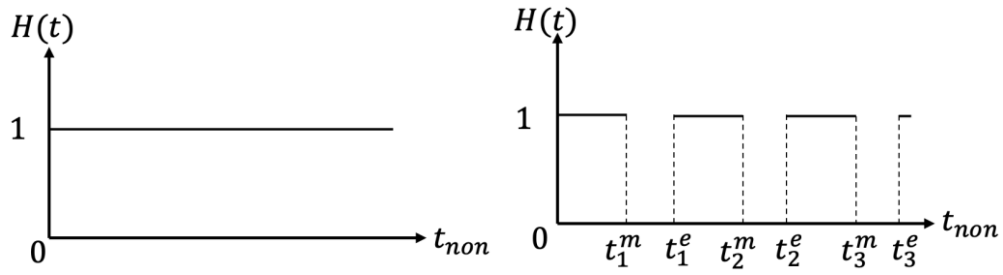

(a) (b)

Fig. 2 Schematic of continuous and pulsed laser sources, as shown in subfigures (a) and (b), respectively. t_{non} is the dimensionless time

For a pulsed laser source as shown in Fig. 2(b), when $t_i^e \le t \le t_{i+1}^m$ $H(t) = 1$ otherwise $H(t) = 0$. t_i^e denotes the end time of the i^{th} cycle period. If t_i^e is not the final end time of the simulation, t_i^e also corresponds to the start time of the $(i+1)^{th}$ cycle. For fixed period situations, a period length is computed through $t_{i+1}^e - t_i^e$. t_{i+1}^m is a time step within the $(i+1)^{th}$ cycle, used to adjust the duty cycle which is calculated by $(t_{i+1}^m - t_i^e)/(t_{i+1}^e - t_i^e)$.

VALIDATION CASES

In this section, several single-track validation cases are presented by comparing the simulated and experimental melt-region cross-sectional dimensions. Fig. 3 briefly describes the simulation model. The computational domain is defined as $x \in [-W_d/2, W_d/2]$, $y \in [0, D_g + D_s]$ and $z \in [0, L_d]$. L_d, W_d denote the length and width of the whole computational domain. D_g, D_s denote the initial depth of gas and material phases before the simulation starts. In this paper, $L_d = 1000$ μm and $D_g = 200$ μm are applied to all cases, and W_d, D_s may vary from case to case. The scanning laser starts at $x = 0, z =$100 μm and ends at $x = 0, z = 900$ μm, with a total scanning distance of 800 μm. The physical properties of copper and SS 316L are provided in Table 1. The universal gas constant is $R = 8.341$ J K^{-1} mol^{-1}.

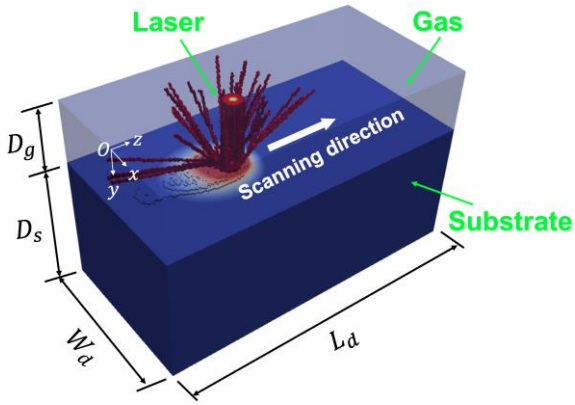

Fig. 3 Visualization of the numerical model including dense material and gas phases

Table 1 Physical properties of Copper and SS 316L used in simulations.

Parameters	Symbol	Copper	SS 316L
Kinematic viscosity ($m^2\ s^{-1}$)	ν_1	5.3×10^{-7}	7.64×10^{-7}
Density ($kg\ m^{-3}$)	ρ_1	7800	7870
Thermal conductivity ($kg\ m\ s^{-3}\ K^{-1}$)	k_1	200	$10.829 + 0.0095T$
Specific heat ($J\ kg^{-1}\ K^{-1}$)	c_1^p	495	$618.5 + 0.067T$
Solidus temperature (K)	T_1^s	1335	1658
Liquidus temperature (K)	T_1^l	1337	1723
Evaporation temperature (K)	T^v	3220	3090
Latent heat of fusion ($J\ kg^{-1}$)	L_1^f	2.06×10^5	2.7×10^5
Latent heat due to vaporization ($J\ kg^{-1}$)	L^v	4.69×10^6	2.45×10^6
Thermal expansion coefficient (K^{-1})	β_1	5.85×10^{-5}	5.8×10^{-5}
Surface tension ($J\ m^{-2}$)	σ	1.304	1.6
Temperature derivative of tension ($J\ m^{-2}\ K^{-1}$)	$d\sigma/dT$	-2.86×10^{-4}	-8×10^{-4}
Vapor pressure ($J\ m^{-3}$)	p_0	1.01×10^5	1.01×10^5
Molar mass ($kg\ mol^{-1}$)	M	0.064	0.05593

An infrared laser with the wavelength of 1070 nm is initially applied to the position defined by Eq. (14) with $b_g = 0$ and $l_g = 100$ μm, moving at a prescribed speed v. When presenting the results, for clarity, we represent the width (W) and depth (D) of the melt region in the manner as shown in Fig. 4.

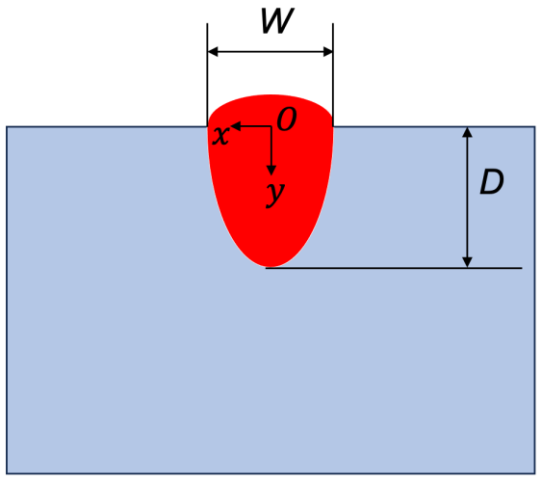

Fig. 4 Dimension denotation of melt-region width (*W*) and depth (*D*)

CONTINUOUS GAUSSIAN LASER ON COPPER

The first validation case is a continuous 400 W Gaussian laser applied on a copper plate. A hexahedral cubic mesh with a cell sidelength of 5 μm is used to discretize the numerical model, which is fine enough to achieve high accuracy according to reference [26]. The laser scanning speed is set to $v = 0.5$ m/s. The laser spot radius is 31 μm. The laser shape is computed using Eqs. (13) and (14), and the relevant parameters are presented in Table 2 as G1. The shape is shown as S:100-0-D1 in Fig. 1. A couple of absorption rates of energy are used to conduct the sensitivity analysis of the melt-region dimension with respect to absorptivity, which is discussed in Section ABSOPTIVITY VS. POWER IN COPPER.

Table 2 Value of required parameters for computing laser beam shapes using Eqs. (13) and (14).

Label	Power ratio	a_r	σ_c (μm)	σ_r (μm)	μ_{R1} (μm)	μ_{R2} (μm)	ω
G1	100-0	0	21.92	–	0	–	–
G2	100-0	0	31.82	–	0	–	–
R1	20-80	0.94	29.53	16.60	0.41	62.94	0.295

Fig. 5(a) compares cross-sections of the simulated and experimental melt regions. Here the local absorption rate is $\eta = 15\%$ in the simulation. Table 3 provides the specific values of the width and depth of the cross section, as Labelled Gaussian. Measured experiment results are referenced from the literature [35], and two sets of reference data are available for each case. Fig. 5(a) only plots one of the two experimental results, and from Table 3 it is seen that the simulated results are within the range of these two sets of values. Note that a particle powder layer with a thickness of 90 μm is added on the substrate surface in the experiment of the paper [35], but considering the computational efficiency we do not include powder in the

simulation. Thus, here we only discuss the penetration dimension without the region above the initial interface.

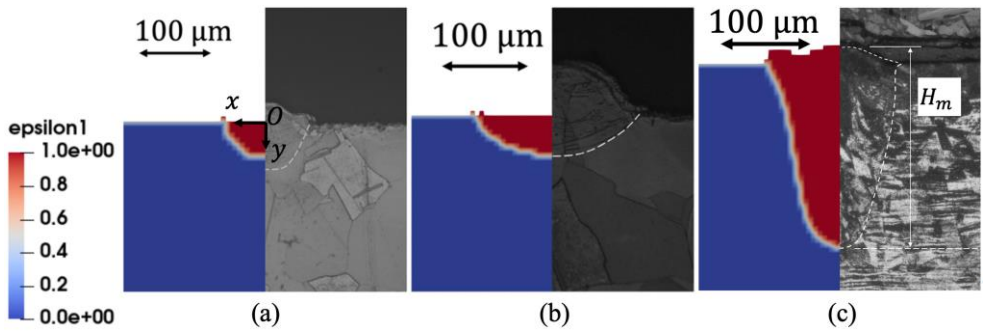

Fig. 5 Cross sections of the melt regions under (a) continuous Gaussian and (b) continuous ring-shaped laser beams on copper, and (c) a pulsed Gaussian laser beam on SS 316L. The left part is the simulation result, and the right is the experimental result. Subfigure (a): 400 W power, $\eta = 15\%$ absorption rate, 0.5 m/s scanning speed, 90×35 μm^2 $(W \times D)$ simulated dimension, and 133×62 μm^2 $(W \times D)$ experimental dimension. Subfigure (b): 1300 W power, $\eta = 3.6\%$ absorption rate, 20-80 core-ring power ratio, 0.5 m/s scanning speed, 170×45 μm^2 $(W \times D)$ simulated dimension, and 211×45.1 μm^2 $(W \times D)$ experimental dimension. Subfigure (c): 260 W power, 6500 Hz frequency, 0.325 m/s scanning speed, and dimensions are given in Table 4; H_m denotes the total height of the melt region.

Table 3 Width and depth of the melt regions under continuous Gaussian and 20-80 ring-shaped beams on copper. RExp denotes the referenced experimental data measured in the literature [34-35], and 1 and 2 represent the value measured at two positions.

Label	Width (µm)			Depth (µm)		
	RExp-1	RExp-2	Simulation	RExp-1	RExp-2	Simulation
Gaussian	133 [35]	62 [35]	90	62 [35]	15 [35]	35
Ring-shaped	211.0 [34]	187.6 [34]	170	36.6 [34]	45.1 [34]	45

SPATIAL BEAM SHAPING: CONTINUOUS RING-SHAPED LASER ON COPPER

The second case is to validate the application of spatial laser beam shaping on copper. A 1300 W ring-shaped beam, with the scanning speed of 0.5 m/s and the core-ring power ratio of 20-80, is applied in this case. The laser shape is computed using Eqs. (13) and (14), and the relevant parameters are presented in Table 2 as R1. The shape is shown as S:20-80 in Fig. 1.

A couple of absorption rates are used to conduct the sensitivity analysis of melt-region dimension with respect to absorptivity, see Section ABSOPTIVITY VS. POWER IN COPPER. Fig. 5(b) and Table 3 give a comparison of simulated and experimental [34] results. The good agreement of the penetration dimension is reached when the absorption rate is $\eta =$

3.6%. Here we do not model the particle powder layer which is included in the reference experiment [34].

TEMPORAL BEAM SHAPING: PULSED GAUSSIAN LASER ON STAINLESS STEEL 316L

The third validation case is a temporal beam shaping for SS 316L. Since there are few experimental studies on pulsed PBF-LB on metals in the literature for reference, we conducted a related single-track remelting experiment using our open-architecture PBF-LB machine developed at DTU, Lyngby [36].

Experimental Setup

Temporal beam shaping is achieved using a 250 W Gaussian infrared laser with a duty cycle of 50%, a cycle length of 153.846 μs corresponding to a switching frequency of 6500 Hz. The spot diameter of the laser is 90 μm, moving at a constant speed of 0.325 m/s. A single track with a length of 20 mm is fabricated on a SS 316L substrate with the dimension of $80 \times 10 \times 1$ mm^3 in a nitrogen atmosphere.

To observe the transverse section of the melt region, three samples are extracted from various locations along the scanning direction. These samples are then embedded in a polyfast resin. Grinding was performed using silicon carbide papers ranging from grit 500 to 4000, followed by polishing with diamond suspensions of 3 μm and 1 μm. Final polishing is conducted using a colloidal silica suspension (OP-S). The polished samples are etched with Kalling reagent-2 for 15 seconds. Optical microscopy is performed using a Carl Zeiss Axio Vert A1 microscope to characterize the microstructure. Melt-region dimensions are characterized in terms of width (W), height (H_m), and depth (D), with their definition illustrated in Figs. 4 and 5(c). The result data are presented in Table 4.

Table 4 Dimension of the melt region under 6500 Hz pulsed Gaussian laser on SS 316L.

	Width (μm)	**Height (μm)**	**Depth (μm)**
Experiment	133 ± 11	223 ± 2	200 ± 2
Simulation	150	220	200

Numerical Implementation

In the simulation, the laser beam shape is computed using Eqs. (13) and (14), with the parameter corresponding to G2 in Table 2. The shape is shown as S:100-0-D2 in Fig. 1. The pulsed configuration matches that used in the experiment. The resulting melt-region profile is shown in Fig. 5(c), and the corresponding dimension data are provided in Table 4. Since no particle powder is involved in either the experimental or simulated models for this remelting case, the total cross-sectional height, from the bottom to the top, is also compared, in addition

to the penetration dimension. The results demonstrate that the simulation achieves high accuracy.

DISCUSSION

ABSOPTIVITY VS. POWER IN COPPER

Considering the high thermal conductivity of copper, we apply a series of laser absorption rates (η) to approach the experimental results in both the Gaussian (absorptivity range of 5% to 21%) and ring-shaped (absorptivity range of 2.2% to 4.8%) validation cases. Figs. 6(a) and 6(b) present the relative deviation of the width and the depth of the transverse melt-region section for both cases. The deviation is calculated by

$$\Delta_r = \frac{\phi - \phi^{ref}}{\phi^{ref}}, \tag{15}$$

where ϕ represents the simulated width and depth, and ϕ^{ref} corresponds to the referenced experiment results. Since the referenced experiment gives two sets of data for each case as shown in Table 3, if ϕ is greater than the larger experimental result, then ϕ^{ref} takes the larger value of the two experimental results; if ϕ is less than the smaller experimental result, then ϕ^{ref} takes the smaller value; if ϕ is within the range of the two experimental results, then we set $\Delta_r = 0$. From Figs. 6(a) and 6(b), it is observed that the width and depth both nonlinearly increase with the absorptivity increasing.

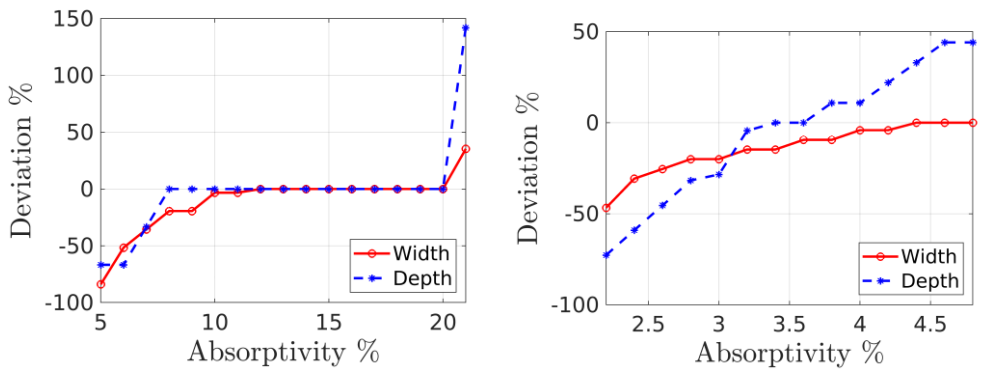

(a) (b)

Fig. 6 Deviation (Δ_r) of cross-section dimension of melt region of copper under continuous (a) Gaussian and (b) 20-80 ring-shaped laser beams for the validation cases

Width varies less with absorptivity than the depth, especially for the ring-shaped cases. This is because that the melt-pool width is greatly limited by the high thermal conductivity of copper and the laser spot size, while the depth is greatly affected by the depression formed by recoil pressure, which is also found in literature [35]. To further explore the influence of power on copper melt-pool dynamics, we extract melt pools at absorptivity of 5%, 15%, 21% under the continuous Gaussian laser irradiation, see Fig. 7. When a small amount of energy is absorbed ($\eta = 5\%$), there is almost no material melted, see Fig. 7(a); when a relatively moderate amount of energy is absorbed, the conduction mode appears, characterized by a round melt pool without noticeable depression, see Fig. 7(b); and when a large amount of energy is absorbed, the keyhole forms, see Fig. 7(c). The keyhole can lead to multiple reflections of the laser rays, significantly increasing the global energy absorption. This is observed in Fig. 6(a) by an increase in melt-region depth, when the local absorption rate η slightly increases from 20% to 21%.

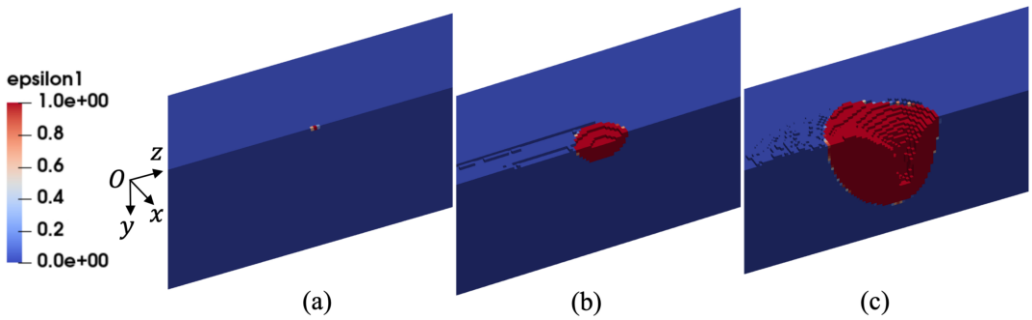

Fig. 7 Bird-eye view of melt pool of copper under the 400 W continuous Gaussian laser, with the absorptivity of (a) $\eta = 5\%$, (b) $\eta = 15\%$, (c) $\eta = 21\%$

SPATIAL AND TEMPORAL BEAM SHAPING EFFECTS ON MELT POOL

By comparing the experimental results in Figs. 5(a) and 5(b), it can be seen that the ring-shaped laser beam makes the melt region relatively shallower and wider than that formed by a pure Gaussian laser. This is because the ring-shaped beam distributes a smaller proportion of laser power to the center, decreasing the average intensity in this case. Such spatial beam shaping helps avoid excessive power concentration in the center, reducing vaporization effects, thereby promoting a stable melting which is observed by comparing the material deposition surfaces in Figs. 8(a) and 8(b). The surface deposited under the ring-shaped laser is smoother and flatter.

Fish-scale patterns appear on the deposition surface under pulsed laser irradiation on copper, as shown in Fig. 8(c). These patterns result from multiple discrete melt pools formed during PBF-LB, which partially overlap with one another. Fish-fin patterns are also observed on the SS 316L deposited surface, as shown in Fig. 8(d). Note that in the case of Fig. 8(c), temporal

beam shaping is achieved using a 400 W pulsed Gaussian infrared laser with a duty cycle of 50%, a cycle length of 153.846 μs corresponding to a switching frequency of 6500 Hz. The spot diameter of the laser is 62 μm, the same as in the continuous Gaussian validation case, and it moves at a constant speed of 0.5 m/s. The case in Fig. 8(d) is taken from the above temporal beam shaping validation case.

Comparing Figs. 8(a) and 8(c), the pulsed melt region in Fig. 8(c) is smaller in size even though the same power and beam shape are applied in both cases, and the pulsed laser technique allows for more controlled and refined melting, making it suitable for high-precision applications. A hump is observed during the PBF-LB process of SS 316L but not in copper, as shown in Figs. 8(c) and 8(d). This is attributed to the lower thermal conductivity of SS 316L, which leads to slower heat dissipation. Additionally, stronger Marangoni effects in SS 316L, i.e., the larger magnitude of the temperature derivative of surface tension (as shown in Table 1), promotes localized accumulation of molten material, increasing the likelihood of the hump formation.

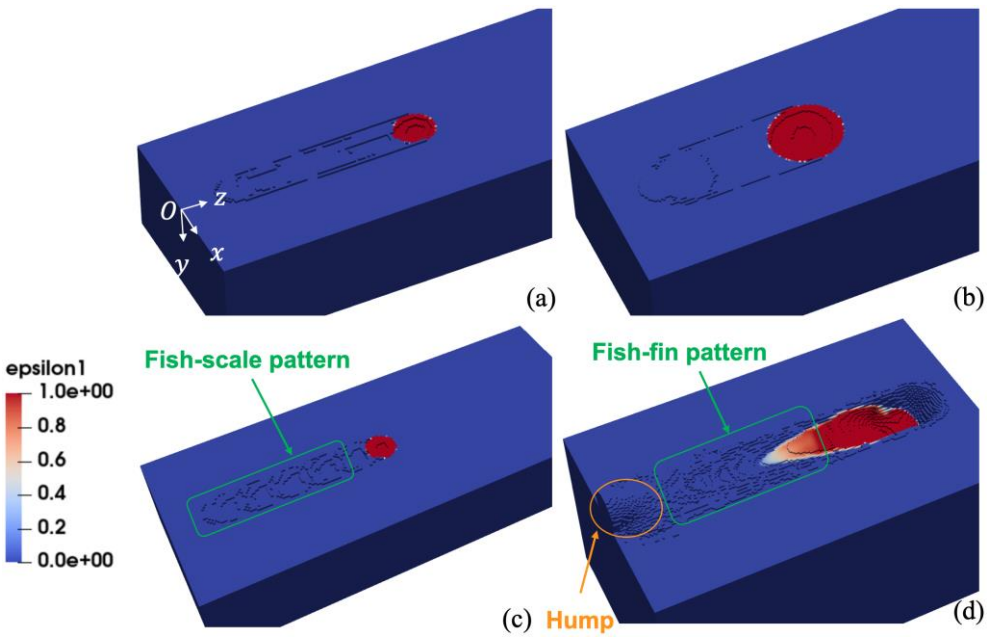

Fig. 8 Bird-eye view of material deposition surface during PBF-LB. (a) Continuous Gaussian laser on copper. (b) Continuous 20-80 ring-shaped laser on copper. (c) Pulsed Gaussian laser on copper. (d) Pulsed Gaussian laser on SS 316L

CONCLUSION

This work extends the open-source PBF-LB solver laserBeamFoam to enable simulation of both spatial and temporal beam shaping in metal additive manufacturing. The implementation is validated against experimental results for continuous Gaussian and ring-shaped laser beams on copper, as well as pulsed Gaussian laser beams on stainless steel 316L (SS 316L), with good agreement in melt-region cross-sectional profiles. Based on a sensitivity analysis of copper's laser absorption behavior, the mechanism behind the nonlinear increase in melt-region dimension with rising absorbed energy is investigated. It is shown that the keyhole formation under high-power irradiation may significantly increase the number of laser beam reflections and energy absorption. Compared to the continuous pure Gaussian irradiation, the ring-shaped beam produces more stable and uniform melting, while pulsed laser irradiation tends to generate fish-scale or fish-fin patterns on the deposited surface.

This work currently considers only one situation each for spatial and temporal beam shaping. In future studies, the effects of varying parameters such as core-ring power ratio, duty cycle, and switching frequency on melt-pool dynamics will be explored. The particle powder layer will also be added in the simulation to approximate the real situation.

ACKNOWLEDGEMENTS

The work is funded by the EU project - GlobalAM (Grant No. 113436) and the Danish-funded project - MicroAM (Grant No. MicroAM-VIL54495). This work has been conducted at Department of Civil and Mechanical Engineering, Section for Manufacturing Engineering. Special thanks are given to Thomas Flint for his support with the laserBeamFoam code.

References

[1] H. REN, X. TIAN, D. LIU, J. LIU and H. WANG: 'Microstructural evolution and mechanical properties of laser melting deposited Ti–6.5Al–3.5Mo–1.5Zr–0.3Si titanium alloy', *Transactions of Nonferrous Metals Society of China*, vol. 25, no. 6, pp. 1856-1864, Jun. 2015, doi: 10.1016/S1003-6326(15)63792-X.

[2] L. C. ZHANG, D. KLEMM, J. ECKERT, Y. L. HAO and T. B. SERCOMBE: 'Manufacture by selective laser melting and mechanical behavior of a biomedical Ti–24Nb–4Zr–8Sn alloy', *Scr. Mater.*, vol. 65, no. 1, pp. 21-24, Jun. 2011, doi: 10.1016/j.scriptamat.2011.03.024.

[3] J. O. MILEWSKI: 'Additive manufacturing of metals: from fundamental technology to rocket nozzles, medical implants, and custom jewelry', *Springer Series in Materials Science*, vol. 258, 2017, pp. 37-44.

[4] H. JASAK, A. JEMCOV and Z. TUKOVIC: 'OpenFOAM: a C++ library for complex physics simulations', In: *International Workshop on Coupled Methods in Numerical Dynamics*, IUC, Dubrovnik, Croatia, 2007, pp. 1-20.

[5] H. B. BINGHAM, P. S. LARSEN and V. A. BARKER: 'Computational Fluid Dynamics: lecture note for course no. 41317', *Unpublished Note*, Technical University of Denmark, 2018.

[6] D. Q. ZHANG, Q. Z. CAI, J. H. LIU, L. ZHANG and R. D. LI: 'Select laser melting of W–Ni–Fe powders: simulation and experimental study', *The International Journal of Advanced Manufacturing Technology*, vol. 51, no. 5-8, pp. 649-658, Nov. 2010, doi: 10.1007/s00170-010-2641-3.

[7] J. YIN, H. ZHU, L. KE, W. LEI, C. DAI and D. ZUO: 'Simulation of temperature distribution in single metallic powder layer for laser micro-sintering', *Comput. Mater. Sci.*, vol. 53, no. 1, pp. 333-339, Feb. 2012, doi: 10.1016/j.commatsci.2011.09.012.

[8] N. E. HODGE, R. M. FERENCZ and J. M. SOLBERG: 'Implementation of a thermomechanical model for the simulation of selective laser melting', *Comput. Mech.*, vol. 54, no. 1, pp. 33-51, Jul. 2014, doi: 10.1007/s00466-014-1024-2.

[9] L. PARRY, I. A. ASHCROFT and R. D. WILDMAN: 'Understanding the effect of laser scan strategy on residual stress in selective laser melting through thermo-mechanical simulation', *Addit. Manuf.*, vol. 12, pp. 1-15, Oct. 2016, doi: 10.1016/j.addma.2016.05.014.

[10] M. MEGAHED, H.-W. MINDT, N. N'DRI, H. DUAN and O. DESMAISON: 'Metal additive-manufacturing process and residual stress modeling', *Integr. Mater. Manuf. Innov.*, vol. 5, no. 1, pp. 61-93, Dec. 2016, doi: 10.1186/s40192-016-0047-2.

[11] T. F. FLINT, G. PARIVENDHAN, A. IVANKOVIC, M. C. SMITH and P. CARDIFF: 'beamWeldFoam: Numerical simulation of high energy density fusion and vapourisation-inducing processes', *SoftwareX*, vol. 18, p. 101065, Jun. 2022, doi: 10.1016/j.softx.2022.101065.

[12] T. F. FLINT, J. D. ROBSON, G. PARIVENDHAN and P. CARDIFF: 'laserbeamFoam: Laser ray-tracing and thermally induced state transition simulation toolkit', *SoftwareX*, vol. 21, p. 101299, Feb. 2023, doi: 10.1016/j.softx.2022.101299.

[13] T. F. FLINT, J. D. ROBSON, P. ESMATI, N. GRILLI, G. PARIVENDHAN and P. Cardiff: 'Version 2.0 – LaserbeamFoam: Laser ray-tracing and thermally induced state transition simulation toolkit', *SoftwareX*, vol. 25, p. 101612, Feb. 2024, doi: 10.1016/j.softx.2023.101612.

[14] A. I. LVOVSKY: 'Fresnel equations', *Encyclopedia of Optical Engineering*, vol. 27, pp. 1-6, 2013.

[15] T. F. FLINT, L. SCOTTI, H. C. BASOALTO and M. C. SMITH: 'A thermal fluid dynamics framework applied to multi-component substrates experiencing fusion and vaporisation state transitions', *Commun. Phys.*, vol. 3, no. 1, p. 196, Nov. 2020, doi: 10.1038/s42005-020-00462-7.

[16] S. B. BOYDEN and Y. ZHANG: 'Temperature and wavelength-dependent spectral absorptivities of metallic materials in the infrared', *J. Thermophys. Heat Trans.*, vol. 20, no. 1, pp. 9-15, Jan. 2006, doi: 10.2514/1.15518.

[17] W. E. ALPHONSO, M. BAYAT and J. H. HATTEL: 'Comparison between green and infrared laser in Laser Powder Bed Fusion of pure copper through high fidelity numerical modelling at meso-scale', In: *13th International Seminar Numerical Analysis of Weldability*, Graz, Austria, 2023, pp. 21-28.

[18] L. GARGALIS *et al.*: 'Determining processing behaviour of pure Cu in laser powder bed fusion using direct micro-calorimetry', *J. Mater. Process Technol.*, vol. 294, p. 117130, Aug. 2021, doi: 10.1016/j.jmatprotec.2021.117130.

[19] W. E. KING *et al.*: 'Observation of keyhole-mode laser melting in laser powder-bed fusion additive manufacturing', *J. Mater. Process Technol.*, vol. 214, no. 12, pp. 2915-2925, Dec. 2014, doi: 10.1016/j.jmatprotec.2014.06.005.

[20] G. NORDET *et al.*: 'Absorptivity measurements during laser powder bed fusion of pure copper with a 1 kW cw green laser', *Opt. Laser Technol.*, vol. 147, p. 107612, Mar. 2022, doi: 10.1016/j.optlastec.2021.107612.

[21] E. SANTECCHIA *et al.*: 'Microstructural features induced by the Gaussian laser beam shape on 316L stainless steel thin-walled samples fabricated by directed energy deposition', *Progress in Additive Manufacturing*, Mar. 2025, doi: 10.1007/s40964-025-01028-1.

[22] J. GRUNEWALD, J. REIMANN and K. WUDY: 'Influence of ring-shaped beam profiles on spatter characteristics in laser-based powder bed fusion of metals', *J. Laser Appl.*, vol. 35, no. 4, Nov. 2023, doi: 10.2351/7.0001153.

[23] J. D. PEREZ-RUIZ *et al.*: 'Laser beam shaping facilitates tailoring the mechanical properties of IN718 during powder bed fusion', *J. Mater. Process Technol.*, vol. 328, p. 118393, Jul. 2024, doi: 10.1016/j.jmatprotec.2024.118393.

[24] A. EBRAHIMI, M. SATTARI, A. BABU, A. SOOD, G.-W. R. B. E. ROMER and M. J. M. HERMANS: 'Revealing the effects of laser beam shaping on melt pool behaviour in conduction-mode laser melting', *Journal of Materials Research and Technology*, vol. 27, pp. 3955-3967, Nov. 2023, doi: 10.1016/j.jmrt.2023.11.046.

[25] S. A. KHAIRALLAH, A. T. ANDERSON, A. RUBENCHIK and W. E. KING: 'Laser powder-bed fusion additive manufacturing: Physics of complex melt flow and formation mechanisms of pores, spatter, and denudation zones', *Acta Mater.*, vol. 108, pp. 36-45, Apr. 2016, doi: 10.1016/j.actamat.2016.02.014.

[26] M. BAYAT, V. K. NADIMPALLI, D. B. PEDERSEN and J. H. HATTEL: 'A fundamental investigation of thermo-capillarity in laser powder bed fusion of metals and alloys', *Int. J. Heat Mass Transf.*, vol. 166, p. 120766, Feb. 2021, doi: 10.1016/j.ijheatmasstransfer.2020.120766.

[27] M. BAYAT *et al.*: 'Exploring spatial beam shaping in laser powder bed fusion: High-fidelity simulation and in-situ monitoring', *Addit. Manuf.*, vol. 93, p. 104420, Aug. 2024, doi: 10.1016/j.addma.2024.104420.

[28] F. GALBUSERA, L. CAPRIO, B. PREVITALI and A. G. DEMIR: 'The influence of novel beam shapes on melt pool shape and mechanical properties of LPBF produced Al-alloy', *J. Manuf. Process*, vol. 85, pp. 1024-1036, Jan. 2023, doi: 10.1016/j.jmapro.2022.12.007.

[29] Q. HAYAT *et al.*: 'Elucidating the effect of circular and tailing laser beam shapes on keyhole necking and porosity formation during laser beam welding of aluminum 1060 using a multiphysics computational fluid dynamics approach', *J. Laser. App.l*, vol. 35, no. 4, Nov. 2023, doi: 10.2351/7.0001150.

[30] V. K. NADIPALLI, S. A. ANDERSEN, J. S. NIELSEN and D. B. PEDERSEN: 'Considerations for interpreting in-situ photodiode sensor data in pulsed mode laser powder bed fusion', In: *Joint Special Interest Group Meeting between Euspen and ASPE Advancing Precision in Additive Manufacturing*, Nantes, France, 2019, pp. 66-69.

[31] M. BAYAT, V. NADIPALLI and J. Hattel: 'Multiphysics simulation of thermal and fluid dynamics phenomena during the pulsed laser powder bed fusion process of 316-L steel', In: *17th UK Heat Transfer Conference*, Manchester, UK, 2022, pp. 1-6.

[32] M. ZHENG *et al.*: 'Surface morphology evolution during pulsed selective laser melting: Numerical and experimental investigations', *Appl. Surf. Sci.*, vol. 496, p. 143649, Dec. 2019, doi: 10.1016/j.apsusc.2019.143649.

[33] C. W. HIRT and B. D. NICHOLS: 'Volume of fluid (VOF) method for the dynamics of free boundaries', *J. Comput. Phys.*, vol. 39, no. 1, pp. 201-225, Jan. 1981, doi: 10.1016/0021-9991(81)90145-5.

[34] A. BAUCH, P. KOHLWES and I. Kelbassa: 'Laser powder bed fusion of pure copper using ring-shaped beam profiles', *J. Laser. Appl.*, vol. 36, no. 4, Nov. 2024, doi: 10.2351/7.0001562.

[35] A. BAUCH and D. HERZOG: 'Influence of temperature and beam size on weld track shape in laser powder bed fusion of pure copper using near-infrared laser system', *J. Laser. Appl.*, vol. 36, no. 1, pp. 1-9, Feb. 2024, doi: 10.2351/7.0001118.

[36] M. B. KJER, V. K. NADIMPALLI, C. L. BUDDEN and D. B. PEDERSEN: 'Applying systems engineering principles to develop an open source laser based metal powder bed fusion system', *Rapid Prototyp J.*, vol. 30, no. 9, pp. 1911-1928, Oct. 2024, doi: 10.1108/RPJ-12-2023-0422.